Micromechanics and strength of agglomerates produced by spray drying

JCIS Open 9 (2023) 100068

Contents lists available at ScienceDirect

JCIS Open

journal homepage: www.journals.elsevier.com/jcis-open

Micromechanics and strength of agglomerates produced by spray drying

Lorenzo Vasquez Giuliano [a], Antonio Buffo [a], Marco Vanni [a], Graziano Frungieri [b,*]

[a] Department of Applied Science and Technology, Politecnico di Torino, Corso Duca Degli Abruzzi 24, 10129, Torino, Italy
[b] Chair of Process Systems Engineering, TUM School of Life Sciences, Technical University of Munich, Gregor-Mendel-Straße 4, 85354, Freising, Germany

ARTICLE INFO

Keywords:
Spray drying
Péclet number
Droplet scale simulations
Discrete element method
Breakup
Fluid dynamic stress
Stokesian dynamics

ABSTRACT

Colloidal suspension spray drying is often used as a route to produce micrometric agglomerates. The morphology and re-dispersion behavior of such agglomerates under fluid dynamic stress is expected to be strongly affected by the operative conditions at which drying is conducted. Motivated by the emerging research area of fluid-activated drug carriers, in this work we studied numerically both the generation mechanism of agglomerates during spray drying, and their mechanical and fragmentation behavior under fluid dynamics stresses. Capillary forces, Brownian motion and the contact mechanics of the particle-particle bonds were kept into account. Results showed that different spray drying conditions lead to substantially different morphologies and mechanical responses of the agglomerates: compact, uniformly dense clusters are obtained for low Péclet number conditions, hollow clusters, with a void core and a thick crust of contacting colloidal particles are instead formed at high Péclet conditions. We also observed that compact agglomerates are considerably stronger than hollow ones, and exhibit brittle rupture under fluid dynamic stresses. Hollow clusters were seen on the contrary to be looser and to undergo noticeable deformation prior to breakup. Finally, this work aims at providing the information needed for selecting spray drying conditions when aiming at a specific morphology and/or re-dispersability properties of colloidal agglomerates.

1. Introduction

Spray drying is a process often used for producing agglomerates starting from a liquid suspension of small colloidal particles. In this process, the liquid suspension is atomized by flowing through a nozzle, it is brought in contact with a hot drying gas, and the suspension droplets generated upon atomization finally undergo evaporation, returning dry large agglomerates composed of contacting smaller primary particles. The process has found application in a number of fields, including, among others, the synthesis of pharmaceutical products [1–5], the manufacturing of ceramic powders [6,7], the production of storage supports for lithium ions [8] or the fabrication of multi functional textiles [9], and it is an established process in the food industry, where it is used to increase the stability of perishable products [10].

The morphology of the granules produced in a spray drying process depends upon several variables, such as temperature, humidity, dimension of the droplets and primary particles size and shape [11–14]. In this context, a number of theoretical and experimental studies reported that the droplet Péclet number plays a key role in determining the granule final morphology. This parameter expresses the ratio between the characteristic Brownian diffusion time of the colloidal particles inside the evaporating droplet and the characteristic droplet evaporation time [15–19]. A high value of the Péclet number is obtained if the diffusion of the primary particles in the droplet is slow compared to the characteristic time of the droplet shrinkage. On the contrary, low Péclet number conditions are encountered when the solvent evaporation is slow and the particle Brownian motion is intense, such that the concentration of particles in the droplet is kept homogeneous throughout the drying process. However, also other phenomena may play a role in determining the agglomerate final structure, such as the buckling instability [20], the failure of some particle-particle contacts, which can possibly lead to the formation of fines [21–23] or the presence of particles with different sizes which can result in the formation of hierarchical structures [24,25].

Different approaches can be adopted to study the solid phase dynamics during a spray-drying process. Some rely on a population balance model, linked to energy and mass transport equations, to follow the solid phase kinetics of nucleation and growth [26–28]. Although this method can provide some insights in the morphology of the produced granules, it

Abbreviations: CDF, Cumulative distribution function; DEM, Discrete element method; FTS, Force-Torque-Stresslet; JKR, Johnson-Kendall-Roberts; SD, Stokesian dynamics.

* Corresponding author.
E-mail address: graziano.frungieri@tum.de (G. Frungieri).

https://doi.org/10.1016/j.jciso.2022.100068
Received 31 July 2022; Received in revised form 5 October 2022; Accepted 14 November 2022

cannot reach the level of structural details that discrete element method (DEM) simulations are able to return [29,30]. By DEM simulations one can in fact track the individual motion of each particle, as it interacts with the other particles and the fluid phase, and obtain finally a full characterization of the granule morphology. By DEM simulations, coupled with a computational fluid dynamic code, Breinlinger et al. [29] studied the effect of the surface tension on the spray drying process. In their case, the Herzian theory was used to count for the particle-particle interactions. Similarly, Zellmer et al. [24] studied the clustering of electrostatically stabilized particles with size that followed a bimodal distribution. They used the Mindlin theory for describing the particle-particle contact and, by parameter tuning, obtained a good agreement with experimental results. In their case, the droplet internal flow was neglected, since this was considered of little importance in a shrinking droplet where the primary driving force for aggregation is the receding surface. In a similar way, by tuning the parameters of a DEM code incoporating a simple repulsion model, Jabłczyńska et al. [25] managed to obtain a good qualitative agreement between DEM predictions and experimental results.

Some applications require the produced granules to be able to deagglomerate into primary particles or fragments smaller than the original granule [31–34]. Re-dispersability is sometimes obtained by including in the spray-dried suspension a water-soluble excipient, such as mannitol, which forms bridges interconnecting the particles during the drying stage, but dissolves quickly when the granules are put in contact with water, thus inducing the separation of the primary particles [35]. More commonly, re-dispersion is obtained by the action of hydrodynamic stresses in the absence of binder [36,37]. In this context, a notable research area, where agglomeration and de-agglomeration by viscous forces are of special interest, is for instance the one aimed at the development of drug carriers for treating thrombosis, in which the agglomerates of particles are required to break up in the proximity of the occlusion, where large shear stresses hold [38,39]. In this case, beside the intensity of the shearing force which is determinant in inducing dispersion, a key role is played also by the spatial arrangement of the primary particles within the granules, which strongly affects the distribution of the mechanical stress in the network of contacting primary particles, the breakup occurrence and consequently the fragment size distribution [36,40,41].

The aim of the present work consists in analyzing the effect of the spray drying conditions on the morphology of granules produced with no added binder, and on their ability to undergo deagglomeration in a liquid medium as induced by the fluid-dynamic stresses. We thus aim at linking the conditions required for de-agglomeration with the operating conditions of the spray drying step. Both steps of the analysis, i.e., the generation and the breakup of the granules, were studied by discrete element method simulations, accurately tracking the motion of each single colloidal particle and keeping into account all the relevant particle-particle and fluid mediated particle-particle interactions, including therefore van der Waals forces, contact forces, Brownian motion and the fluid induced stress.

The paper is organized as follows: in Section 2 the computational approaches for simulating both the spray drying process and the fluid induced agglomerate breakup are outlined, in Section 3.1 the morphology of the agglomerates produced by spray drying are characterized at various Péclet conditions, in Section 3.2 the numerical predictions are compared with a continuous model, whereas in Section 3.3 and 3.4 the mechanical response of the agglomerates to the flow field is studied for the different obtained morphologies. Concluding remarks follow in Section 4.

2. Methods

We used discrete element method simulations to study both the generation by spray drying and the breakup of the agglomerates by fluid dynamics stresses. However, even if in the same DEM framework, the approaches used for studying the two steps were significantly different and each reflected the typical features and issues of the process to be simulated.

The spray drying process was examined at the level of a single droplet of suspension evaporating at a constant shrinkage rate with an initial uniform distribution of particles. By running single drop simulations, we did not address therefore the effect of the droplet population polydispersity and the possible coalescence phenomena occurring during the process. The motion dynamics of the suspended particles was modeled through the open-source software *Yade* [42], here modified to take into account the relevant forces acting on the particles during the droplet shrinking, namely the capillary force, the Brownian force and the adhesive forces. Fluid-particle interactions were modeled by considering the Stokes drag force only, with no direct modelling of the particle-particle hydrodynamic interactions. It is believed in fact that agglomeration in a shrinking droplet is driven by the capillary force acting on the particles sitting at the liquid-vapor interface, which, by retracting, pushes the particles towards each other with a force that is largely dominating over the resistance induced by hydrodynamic interactions.

The study of the de-agglomeration behaviour was instead conducted by accurately taking into account hydrodynamic interactions as well as the colloidal interactions between particles. This was done by coupling proper models for the colloidal interactions with the FTS (force-torque-stresslet) formulation of Stokesian dynamics. This was necessary as hydrodynamic interactions between constituent particles are known to seriously influence the restructuring and breakup behaviour of agglomerates [36,43–45].

2.1. Single drop analysis of spray drying

The simulated system consisted of a uniform population of spherical colloidal particles with common radius a and initially uniformly dispersed within a spherical water droplet undergoing evaporation. The temperature in the droplet was assumed to be uniform.

In the DEM, forces and torques acting on particles are calculated in order to evolve their equations of motion. These equations are solved individually for each particle, so the following steps are referred to the computation of the motion of a single sphere. The position of a particle is $\mathbf{x}_p$ and its value at the current time t is $\mathbf{x}_p(t)$. This value is updated for the next timestep as $\mathbf{x}_p(t+\Delta t)$ by a second order integration of the following equation of motion:

$$m\ddot{\mathbf{x}}_p = \sum_i \mathbf{F}_i \tag{1}$$

where $\ddot{\mathbf{x}}_p(t)$ is the particle acceleration, m is the mass of the particle, and the term on the r.h.s. counts for all the forces the particle is subject to.

Viscous force and torque acting on the particles were considered according to the free draining approximation, thus assuming that every particle interacts with the surrounding fluid as if it were alone in the system, thus neglecting all fluid-mediated particle-particle interaction [40,46–48]. Consequently, the viscous force acting on a single primary particle reduces to the Stokes drag force:

$$\mathbf{F}_{\text{drag}} = -6\pi\mu a(\dot{\mathbf{x}}_p - \dot{\mathbf{x}}_l) \tag{2}$$

where μ is the liquid viscosity, a the radius of the primary particle, $\dot{\mathbf{x}}_p$ the linear velocity of the particle and where $\dot{\mathbf{x}}_l$ is the linear velocity of the liquid at the particle coordinates, which, under the condition of stagnant fluid, is equal to zero. Drag torque calculations are similar, but rotational velocities $\boldsymbol{\omega}$ are required:

$$\mathbf{T}_{\text{drag}} = -8\pi\mu a^3(\boldsymbol{\omega}_p - \boldsymbol{\omega}_l) \tag{3}$$

Brownian effects were taken into account by computing the Brownian force acting on each particle as [49]:

$$\mathbf{F}_{\text{Brown}} = \sqrt{\frac{24\,k_B T \cdot 6\pi\mu a}{\Delta t}} \cdot \chi \tag{4}$$

where k_B is the Boltzmann constant, Δt is the fixed timestep between iterations and χ is a three-elements vector where each element is a random number drawn at each iteration from a uniform distribution between -0.5 and $+0.5$. Brownian torque calculations are analogous and are based on the following equation:

$$\mathbf{T}_{\text{Brown}} = \sqrt{\frac{24 k_B T \cdot 8\pi\mu a^3}{\Delta t}} \cdot \chi \tag{5}$$

Additional forces arise from the binary interactions between the primary particles at contact. The contact model used is the elastic-frictional model developed by Cundall and Strack [50] along with a cohesive normal force which was estimated according to the Johnson-Kendall-Roberts (JKR) theory of contact mechanics as [51]:

$$F_{\text{coh}} = F_{\text{po}} = \frac{3}{2}\pi\gamma_s a \tag{6}$$

where γ_s is the superficial energy of the monomers, and where the first equality states that the cohesive force equals the pull-off force F_{po} required to break the bond between the two particles. This model is available as a standard implementation in *Yade* and it is described in detail in the official documentation of the code and in related articles [42,52,53].

A quadratic law was prescribed to describe the reduction in time of the droplet radius R starting from its initial value R_0 [24]:

$$[R(t)]^2 = R_0^2 - k \cdot t \tag{7}$$

from which the total evaporation time τ corresponding to the condition $R(t) = 0$ can be calculated as $\tau = R_0^2/k$. Equation (7) can be obtained from a mass and heat balance of the droplet interaction with the surroundings and predicts a linear decrease of the droplet surface in time. Such a model is fully appropriate for the first stage of drying, where the solvent occupies a major part of the evaporating front, and, as such, the process is similar to the evaporation of a particle-free droplet. However, as observed in previous works [26,54], as drying proceeds, the evaporation rate might be affected by the accumulation of particles on the droplet surface which forces the solvent to diffuse through the void space in-between them. However, even if such a feature can be in principle incorporated in our modeling framework, no established form for describing this secondary stage of drying exists.

As the droplet dries, the solid particles are drawn inwards by capillary forces. The force arising from the interaction between the surface of the droplet and the particles wet by it was modeled as a force oriented toward the center of the spherical droplet whose magnitude, proportional to the wet perimeter of the particle, is given by:

$$F_c = 2\pi\sigma\sqrt{a^2 - (r - R)^2} \tag{8}$$

where σ is the surface tension of the liquid and r the radial coordinate of the particle in a reference system centered at the droplet center of mass (Fig. 1). In principle, the rigorous evaluation of the capillary force should take into account the shape of the meniscus at the solid-liquid contact line and the contact angle. Equation (8) is therefore a simplification that correctly predicts the maximum capillary force ($2\pi a\sigma$) for a fully wettable particle at the interface, and allows for a smooth transition of F_c to zero when the particle becomes completely immersed in the liquid.

We observed that, with the adopted set of parameters, contact forces are strong enough to make post-contact deformations extremely small. Hence, the generated structure is practically rigid, and does not exhibit the substantial restructuring that may occur as a result of significant sliding or rolling phenomena of one particle on another in the secondary part of drying. Under these conditions, the results did not depend on the intensity of the capillary centripetal force, which merely moved the particles towards the center of the droplet without being able to induce substantial rearrangement of the structure after contacts were formed. Based on this observation, we used a surface tension value that is much lower than that of the real liquid-vapor interface. This made the simulations more stable and faster, without affecting the robustness of the predictions.

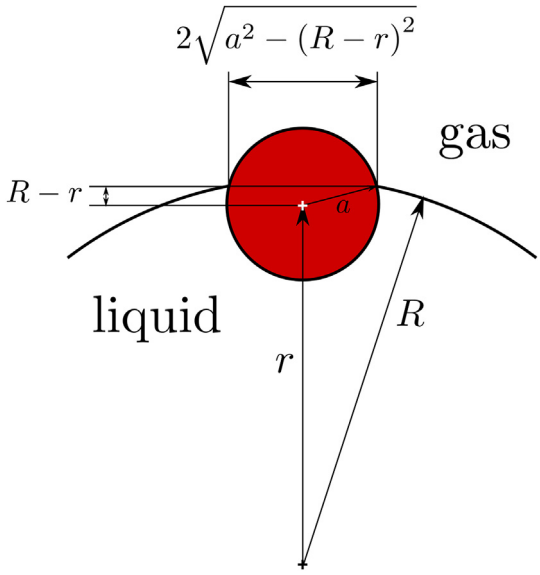

Fig. 1. Primary particle in contact with the droplet surface: estimation of the wet perimeter and capillary force.

In this part of the work lubrication forces and pre-contact van der Waals attraction between particles were both neglected, based on the fact that they have opposite effects on the formation of a particle-particle contact. Lubrication forces tend in fact to keep particles away from each other, whereas van der Waals forces act favoring their contact. Their interplay may play a role in the kinetics of the contact formation, but it is not expected to significantly affect the agglomerate morphology once contacts are formed. Similarly, we did not considered the energy barrier to the contact formation due to the electrostatic repulsion between particles. These were seen to influence the kinetics of formation and buckling of granules [20], however their role should be expected to become less and less important at increasing ionic strength and/or decreasing surface potential of the particles [19]. The parameter values used for the spray drying investigation are listed in Table 1.

2.2. Agglomerate dispersion by Stokesian dynamics

The study of the agglomerate rupture due to viscous stresses requires two improvements in the DEM compared to the model used for simulating the spray drying process. Firstly, the viscous forces, which are responsible for breakage, must be predicted accurately. The free draining approximation used in the first part of the work neglects in fact fluid-mediated particle-particle interactions, which are known to strongly influence the way agglomerates undergo restructuring and breakup [44,45]. Secondly, in this case, it is necessary to accurately compute and track

Table 1
Values of the parameters used for estimating contact forces.

Parameter	Symbol	Value	Units
Particle density	ρ_p	1300	kg m^{-3}
Elastic modulus	E	3.40	GPa
Poisson ratio	ν	0.5	–
Surface tension	σ	$1.75 \cdot 10^{-4}$	N m^{-1}
Superficial energy	γ_s	$4.80 \cdot 10^{-3}$	N m^{-1}

the distribution of the mechanical stresses within the agglomerate structure, in order to ascertain if the critical stress inducing fracture is reached at any particle-particle contact. This effect in the first part of the work was largely neglected because we simulated the formation of granules in which the spatial configuration of the particles was practically frozen after contact. In this second part of the work, for rigorously addressing the deagglomeration phenomenon, we opted for using Stokesian dynamics (SD) [41,55–58], coupled with proper models for describing the colloidal particle-particle interactions [36]. Stokesian dynamics computes, with a low order expansion of the exact solution of the Stokes flow, the hydrodynamic force acting on each primary particle, for any possible particle arrangement. It does not return the flow field inside or around the structure, but indeed this is taken into full account when computing hydrodynamic forces. Thus, Stokesian dynamics completely solves the flow field, even in the inter-particle space between monomers. The boundary condition, i.e. the type of flow field, is imposed at infinite distance from the agglomerate. The domain is unbounded in the standard Stokesian dynamics formulation used here.

We used the Force-Torque-Stresslet formulation of Stokesian dynamics, according to which the relationship between hydrodynamic stresses, relative particle arrangement and particle velocity is given by the following linear system of equations [59]:

$$\mu \begin{bmatrix} R^{\dot{X}F} & R^{\Omega F} & R^{EF} \\ R^{\dot{X}T} & R^{\Omega T} & R^{ET} \\ R^{\dot{X}S} & R^{\Omega S} & R^{ES} \end{bmatrix} \begin{Bmatrix} \dot{\mathbf{x}} - \dot{\mathbf{x}}^{\infty}(\mathbf{x}) \\ \boldsymbol{\omega} - \boldsymbol{\omega}^{\infty}(\mathbf{x}) \\ -\mathbf{E}^{\infty}(\mathbf{x}) \end{Bmatrix} = -\begin{Bmatrix} \mathbf{F} \\ \mathbf{T} \\ \mathbf{S} \end{Bmatrix} \tag{9}$$

where μ is the medium viscosity and where $\mathbf{F} = (\mathbf{f}_1, \ldots, \mathbf{f}_i, \ldots, \mathbf{f}_p)$, $\mathbf{T} = (\mathbf{t}_1, \ldots \mathbf{t}_i, \ldots, \mathbf{t}_p)$ and $\mathbf{S}$ are the hydrodynamic forces, torques and stresslet acting on the p particles composing the agglomerate. The stresslet tensor, symmetric and traceless, is reduced to the equivalent five-component column vector $\mathbf{S} = (S_{xx}, S_{xy}, S_{xz}, S_{yz}, S_{yy})$. The vectors $\dot{\mathbf{x}} = (\dot{\mathbf{x}}_1, \ldots, \dot{\mathbf{x}}_i, \ldots, \dot{\mathbf{x}}_p)$ and $\boldsymbol{\omega} = (\boldsymbol{\omega}_1, \ldots, \boldsymbol{\omega}_i, \ldots, \boldsymbol{\omega}_p)$ are the linear and angular velocities of the primary particles, while $\dot{\mathbf{x}}^{\infty}(\mathbf{x})$ and $\boldsymbol{\omega}^{\infty}(\mathbf{x})$ are the linear and angular velocities of the undisturbed flow field at the particle location $\mathbf{x}$. The rate of strain $\mathbf{E}^{\infty}$ is reported in the same reduced form as the stresslet $\mathbf{S}$. The matrix at the left hand side of Eq. (9), i.e., the resistance matrix, is symmetric and positive definite, and its terms depend only on size and relative positions of the primary particles. The resistance matrix includes two contributions: a first order multipole expansion of the rigorous solution of the fluid velocity gives the far field components, which describe correctly hydrodynamic interactions between particles that are relatively far apart. A near field correction, based on lubrication theory, and added to the far field matrix, was used to correctly reproduce the behavior of the particles that were in relative motion close to each other.

Contact mechanics allowed us to convert the hydrodynamic forces and torques exerted by the fluid on the particles in a distribution of internal contact forces. Such internal forces govern the relative displacement of the particles in the cluster. The mutual configuration of a pair of contacting spherical primary particles has 6 degrees of freedom: one from normal straining, one from twisting, two from shearing and two from bending. A visual representation is shown in Fig. 2. Normal displacement originates from the relative linear velocity of the particles along the interaction axis described by the unit vector $\mathbf{n}$ in the picture; sliding is caused by the relative linear velocity perpendicular to $\mathbf{n}$; twisting originates from the relative rotational velocity along $\mathbf{n}$; bending is caused by the relative rotational velocity components perpendicular to $\mathbf{n}$.

The normal contact force acting between a pair of primary particles was obtained by linearisation of the JKR theory [51], as discussed in the work by Frungieri and Vanni [36]. For a pair of contacting particles the surface-to-surface distance h is related to the force F_n acting along the normal direction. This distance is nil when undeformed particles are just in contact and may become positive or negative due to the deformation of the contact region under traction or compression, respectively. The relationship between h and F_n is as follows:

$$h = \frac{b_0^2}{a}\left(\frac{1+\sqrt{1+F_n/F_{\text{coh}}}}{2}\right)^{1/3} \cdot \left(\frac{1-3\sqrt{1+F_n/F_{\text{coh}}}}{3}\right) \tag{10}$$

where the zero-load contact radius is $b_0 = \left(9\pi\gamma_s a^2(1-\nu^2)/2E\right)$, where γ_s is the surface energy of the solid and where ν and E are respectively the Poisson ratio and the elastic modulus of the primary particles. The cohesive force of the contact, i.e., the largest traction force that the contact can bear, is given by Eq. (6).

When two contacting particles are pulled apart, due to cohesive forces, the contact is preserved up to a positive surface-to-surface distance, referred to as pull-off distance h_{po}, which is the distance at which detachment occurs abruptly:

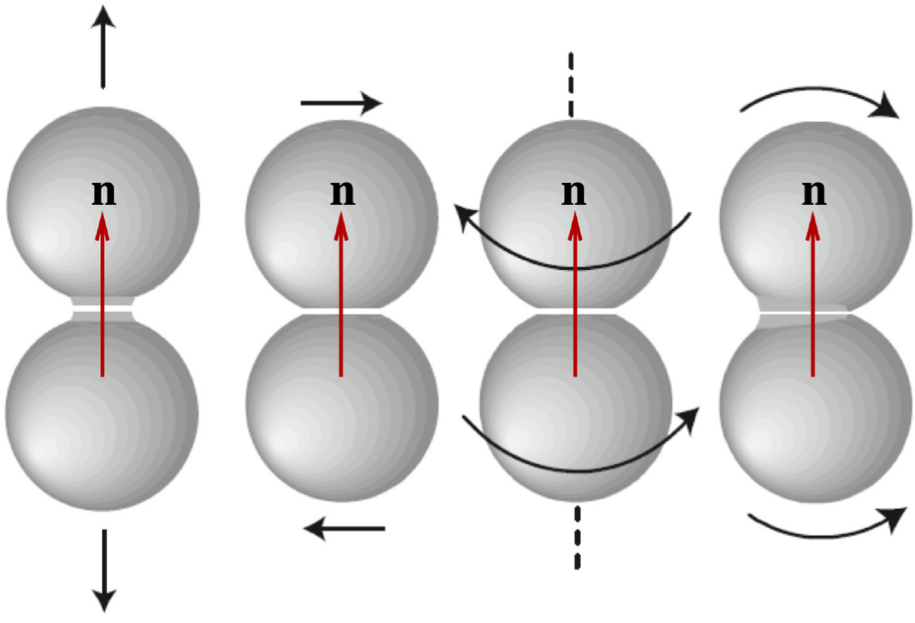

Fig. 2. Relative displacements between contacting spheres. From left to right: normal interaction, sliding, twisting, rolling.

$$h_{\mathrm{po}} = \left(\frac{3\pi^2\gamma_s^2 a(1-\nu^2)^2}{8E^2}\right)^{1/3}. \tag{11}$$

In physical terms it means that, while particles are moving apart, a small neck of material is present at the contact, preventing detachment as long as its length is smaller than h_{po}.

Contact forces and torques related to non-normal interaction (i.e., mutual sliding, rolling and twisting) were calculated by the model by Marshall [60]. The sliding resistance force was calculated using a spring model prescribing that:

$$F_s = \min\left(k_s \int_0^t \mathbf{u}_s(\tau)d\tau \cdot \mathbf{t}_s; F_s^{\mathrm{crit}}\right) \tag{12}$$

where k_s is the sliding stiffness coefficient estimated using the following equation [57]:

$$k_s \approx 3.3\frac{[\pi\gamma_s(1-\nu)]^{1/3}}{2-\nu}\left(\frac{aE}{1+\nu}\right)^{2/3} \tag{13}$$

The term $\mathbf{u}_s$ in Eq. (12) is the component of the particle relative velocity at the contact point aligned with the sliding direction $\mathbf{t}_s$. As long as the tangential force responsible for sliding is lower than the critical value F_s^{crit}, the force can be balanced by the elastic reaction of the contact, which is proportional to the tangential displacement. The critical displacement ξ^{crit}, corresponding to F_s^{crit}, is estimated on the basis of the work of Dominik and Thielens [61]:

$$\xi^{\mathrm{crit}} \approx 0.05\frac{\pi E b_0^2}{2(1+\nu)} \tag{14}$$

where b_0 is the radius of the contact region if no forces are applied, as predicted by the JKR theory.

The twisting resistance torque M_t opposes the relative rotation of two particles around the axis connecting their centers. It was calculated using a relationship similar to the one of Eq. (12) and reads as:

$$M_t = \min\left(k_t \int_0^t \Omega_t(\tau)d\tau; M_t^{\mathrm{crit}}\right), \tag{15}$$

where Ω_t is the relative torsional velocity. The torsional stiffness coefficient k_t is given by:

$$k_t = 6\pi\gamma_s a^2(1-\nu) \tag{16}$$

The critical angular displacement $\varphi_t^{\mathrm{crit}}$, corresponding to the largest torsional torque that can be balanced by the elastic reaction of the contact before the contact point advances, is given by [61]:

$$\varphi_t^{\mathrm{crit}} \approx 0.05\frac{E b_0^3}{18\gamma_s a^2(1-\nu^2)} \tag{17}$$

The rolling resistance torque M_r and stiffness coefficient k_r are defined analogously to the sliding and twisting parameters [61]. In order to distinguish the effect of rolling from other types of motions, the relative rolling velocity $\mathbf{u}_r$ between the two contacting spheres i and j is defined as follows [62]:

$$\mathbf{u}_r = -a(\boldsymbol{\Omega}_i - \boldsymbol{\Omega}_j) \times \mathbf{n} \tag{18}$$

where $\boldsymbol{\Omega}_i$ and $\boldsymbol{\Omega}_j$ are the angular velocities of the two particles and $\mathbf{n}$ the unit vector connecting their centers. The rolling resistance M_r is calculated as

$$M_r = \min\left(k_r\left(\int_0^t \mathbf{u}_r(\tau)d\tau\right) \cdot \mathbf{t}_r; M_r^{\mathrm{crit}}\right) \tag{19}$$

where the term $\mathbf{t}_r$ is the direction of rolling, i.e., the unit vector aligned with the direction of the rolling velocity $\mathbf{u}_r$. The rolling stiffness coefficient k_r and the critical angular displacement $\varphi_r^{\mathrm{crit}}$ were respectively computed as:

$$k_r = 3\pi\gamma_s a^2 \tag{20}$$

$$\varphi_r^{crit} \approx 0.2\frac{b_0}{a} \tag{21}$$

A considerable simplification of the method can be obtained in the limit of small elastic deformations, as discussed by Vanni [57]. In this case the agglomerate can be described as a rigid body in which the relative positions of the primary particles never change and the velocity of each particle can be easily related to the velocity of the center of mass of the agglomerate. Although this assumption causes the loss of some information about the dynamics of restructuring of the agglomerate, it will be employed in the following as a benchmark setup for the more detailed modeling approach just outlined.

3. Results

3.1. Spray drying - Agglomerate characterization

The ratio between the time scale of diffusion and the time scale of droplet evaporation, described by the Péclet number, was seen to have a major influence on the final morphology of the agglomerates. We computed the Péclet number as:

$$Pe = \frac{R_0^2}{\mathcal{D}\tau} \tag{22}$$

where R_0 is the droplet initial radius, τ is the shrinkage time of the droplet, given by the evaporation rate of Eq. (7), and where $\mathcal{D}$ is the diffusion coefficient of the primary particles due to the Brownian motion, which was calculated using the Stokes-Einstein equation:

$$\mathcal{D} = \frac{k_B T}{6\pi\mu a} \tag{23}$$

In Eq. (22), $R_0^2/\mathcal{D}$ can be seen as a characteristic diffusion time of the particles inside the droplet.

The Péclet number is large when diffusion is slow compared to the evaporation velocity: under this condition, the particles were not redistributed in the droplet by Brownian motion and were seen to accumulate at the evaporating front, where they constituted a spherical shell or crust. On the contrary, the Péclet number is low if diffusion is fast compared to the time scale of evaporation: in this case, the concentration of primary particles in the droplet was seen to be kept homogeneous by Brownian motion throughout the evaporation, finally leading to the generation of a homogeneous and compact spherical agglomerate. These observations qualitatively well compare with those reported in Ref. [16], where single drop drying experiments were conducted in an acoustic levitator, and with the ones of Ref. [25] where a conventional spray drying setup was used. The video animations of two sample simulations (at low and large Péclet) are available in the online Supplementary Material of this article.

We quantitatively characterize the different morphologies by computing the radial distribution of the primary particles, the diameter d_c and the crust thickness h_c of the agglomerates. The radial distribution for a sample of agglomerates is presented in Fig. 3 as a cumulative distribution function (CDF), reporting the fraction of particles located at a radial distance from the center of mass of the granule smaller than r. The plot compares the agglomerates generated from three simulations conducted at different Péclet numbers, obtained by varying the shrinkage velocity (principal simulation parameter in Table 2). For the ideal case of $Pe \to \infty$, the diffusion coefficient $\mathcal{D}$ was set to zero. From the CDF and the

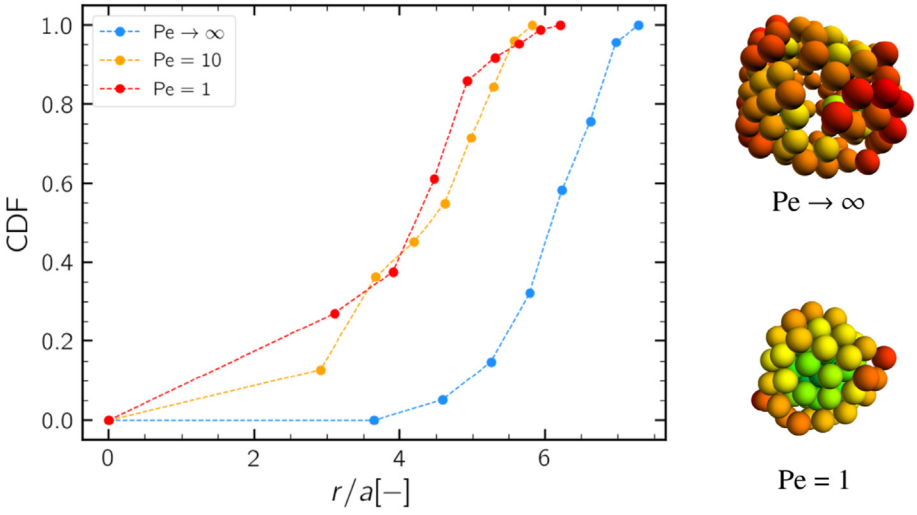

Fig. 3. Cumulative distribution function of the particle radial position in agglomerates obtained for different values of Péclet number. The structures obtained for $Pe \to \infty$ and $Pe = 1$ are also visually depicted. The colormap serves to highlight the difference between the empty core of the cluster obtained for $Pe \to \infty$ and the compact core of the cluster obtained for $Pe = 1$. Green particles are close to the center of mass of the agglomerate, red particles are far from it. (For interpretation of the references to color in this figure legend, the reader is referred to the Web version of this article.)

Table 2
Effect of the Péclet number on the granule morphology. Principal parameters of the simulations and values of agglomerate diameter d_c, crust thickness h_c, and h_c/d_c ratio for a sample of morphologies. In the table, a is the particle radius, R_0 the initial droplet radius, τ the evaporation time, $\mathcal{D}$ the particle diffusivity.

monomers	a [nm]	R_0 [μm]	solid fraction	τ [ms]	$\mathcal{D}$ [m^2/s]	Pe	d_c [nm]	h_c/d_c
115	10	0.215	1.2%	0.21	0	∞	160	0.28
102	10	0.215	1.0%	0.21	$2.2 \cdot 10^{-11}$	10	132	0.43
85	10	0.215	0.9%	2.10	$2.2 \cdot 10^{-11}$	1	132	0.44

picture of the agglomerates, it can be noticed that compact clusters were obtained at low Péclet numbers ($Pe < 10$), while hollow agglomerates with a large internal cavity were observed for $Pe \to \infty$.

As proposed by Jabłczyńska and coworkers [25], the outer radius of a cluster can be defined as the mean distance from the center of mass of 10% of the farthest primary particles plus the radius of one particle; analogously, the inner radius is the mean distance of 10% of the nearest particles minus the radius of one particle. It follows that the cluster diameter d_c is two times the outer radius and the crust thickness h_c is the difference between the outer radius and the inner radius. The ratio h_c/d_c can be used for characterizing the agglomerates: a low value of h_c/d_c means that the agglomerate is shell-shaped with an inner cavity, while the maximum theoretical value of h_c/d_c, which is equal to 0.5, holds for clusters that are compact and homogeneous. The values of the h_c/d_c ratio reported in Table 2 confirms what inferred from the particle radial distribution. For low Péclet numbers h_c/d_c tends to 0.5, meaning that the final agglomerate is compact, whereas for $Pe \to \infty$, h_c/d_c is low, meaning that the final agglomerate is hollow, it has, i.e., a void core and an external crust.

In the production of micrometric granules, the initial droplet radius is often reported to be around 20-50 μm and the shrinkage time to range between 0.01 and 0.1 s. Under these conditions, which are quite frequent in practical drying systems, the Péclet number is always much larger than the unity, even in the presence of extremely small primary particles. For this reason we examined in some detail the behavior of the system in the high Péclet regime focusing, in particular, on the effect of the evaporation time τ on the final shape of the granules. A set of simulations at large Péclet number but with different shrinkage times was performed (Table 3). The radius of the particles and the radius of the droplet are 1 μm and 40 μm respectively, and the volumic solid fraction with respect to the volume of the droplet is around 0.1%. For every condition of the system, five different but equivalent simulations were realized. The results are summarized in Fig. 4, where it can be noticed that both the size (graph a) and the h_c/d_c ratio (graph b) are not affected by the variation of the shrinkage time in the high Pe limit, thus proving that the agglomerate morphology is insensitive to small variations of the drying conditions in this regime.

Table 3
Principal parameters of the simulations for evaluating the effect of the shrinkage time τ in the high Péclet number limit. The number of monomers was around 60 in all simulations.

a [nm]	R_0 [μm]	solid fraction	τ [ms]	$\mathcal{D}$ [m^2/s]	Pe
1000	40	~ 0.1%	3	$2.2 \cdot 10^{-13}$	$2.4 \cdot 10^6$
1000	40	~ 0.1%	6	$2.2 \cdot 10^{-13}$	$1.2 \cdot 10^6$
1000	40	~ 0.1%	12	$2.2 \cdot 10^{-13}$	$6.1 \cdot 10^5$
1000	40	~ 0.1%	18	$2.2 \cdot 10^{-13}$	$4.1 \cdot 10^5$
1000	40	~ 0.1%	25	$2.2 \cdot 10^{-13}$	$2.9 \cdot 10^5$

3.2. Verification of the method for short times

We contrasted our predictions obtained by the single-drop discrete element method simulations with a continuous model which can be deemed as a good approximation of the process in the initial part of the evaporation and in the limit of low particle concentration. In such conditions, in fact, the dynamics of the population of particles can be studied as one would study the evolution of the concentration of a dissolved solute, which inside the shrinking droplet undergoes molecular diffusion.

We assumed the droplet to have an initial radius equal to R_0 and to shrink accordingly to the quadratic law of Eq. (7). The receding velocity v of the evaporating front is therefore given by:

$$v = -\frac{dR}{dt} = \frac{k/2}{R} \tag{24}$$

If $C(r, t)$ is the solute concentration, its evolution in time inside the droplet can be described by the following unsteady diffusion equation [63]:

$$\frac{\partial C}{\partial t} = \frac{\mathcal{D}}{r^2}\frac{\partial}{\partial r}\left(r^2\frac{\partial C}{\partial r}\right) \tag{25}$$

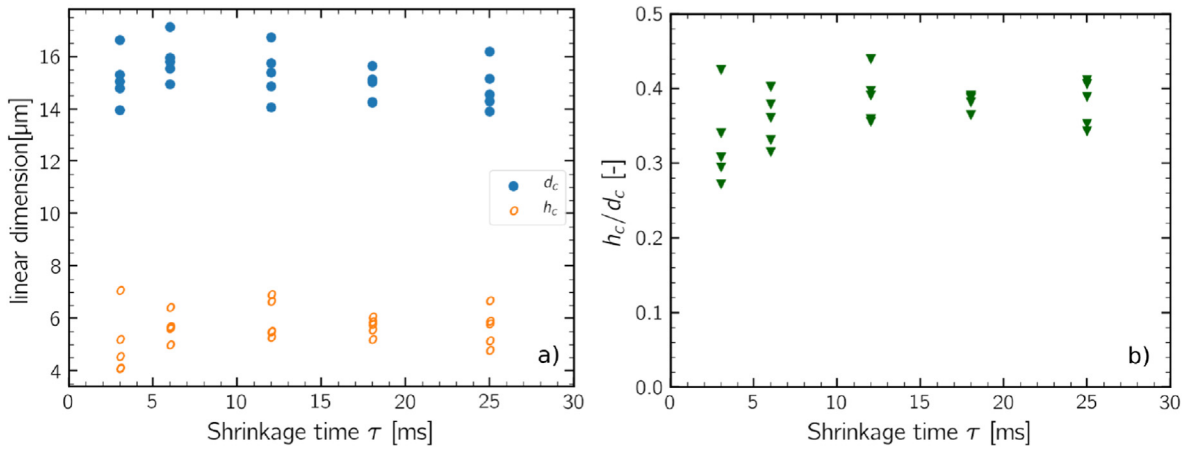

Fig. 4. Values of crust thickness h_c, granule diameter d_c and h_c/d_c ratio for clusters obtained at high Péclet number at varying evaporation time τ. For every τ, five different but equivalent simulations were run. The cluster morphology is not significantly affected by the shrinkage time in the high Péclet number regime.

with boundary conditions at the center of the droplet and at the receding front, respectively defined as:

$$\left[\frac{\partial C}{\partial r}\right]_{r=0} = 0 \tag{26}$$

$$\left[vC - \mathcal{D}\frac{\partial C}{\partial r}\right]_{r=R(t)} = 0 \tag{27}$$

The boundary conditions prescribe therefore that the system has radial symmetry (Eq. (26)), and that the interface is impermeable to the solid, such that the diffusive flux given by the Fick's law balances the flux vC at the outer radius of the droplet (Eq. (27)). We set a uniform initial concentration $C_{(t=0)} = C_0$.

To solve the problem it is convenient to reformulate the equations in term of dimensionless concentration C/C_0, dimensionless time $\theta = kt/R_0^2$ and dimensionless radial position $\rho = r/R(t)$. By doing so, *i*) the moving boundary problem defined by the boundary condition of Eq. (27) is transformed in a fixed boundary problem, where the condition is applied at the constant dimensionless coordinate $\varrho = 1$, and *ii*) the solution depends on a single parameter, the Péclet number $\mathcal{D}/k$. The dimensionless set of equations reads as follows:

$$\frac{\partial \Gamma}{\partial \theta} = -\frac{\rho}{2(1-\theta)}\frac{\partial \Gamma}{\partial \rho} + \frac{D/k}{1-\theta}\left(\frac{2}{\rho}\frac{\partial \Gamma}{\partial \rho} + \frac{\partial^2 \Gamma}{\partial \rho^2}\right) \tag{28}$$

$$\left[\Gamma - 2\frac{D}{k}\frac{\partial \Gamma}{\partial \rho}\right]_{\rho=1} = 0\ ;\ \theta > 0 \tag{29}$$

$$\Gamma(\theta = 0) = 1\ ;\ 0 < \rho < 1 \tag{30}$$

Equation (28) was solved by using a second order finite difference scheme for discretizing the spatial coordinate and by a Runge-Kutta scheme for the time advancement of the solution.

The results of the continuous model for two different values of the Péclet number are reported in Fig. 5 as dashed lines and contrasted with the discrete element method results (solid lines). The graphs reports the number particle concentration profile in the shrinking droplet for three different dimensionless times: $\theta = 0.0$, $\theta = 0.2$ and $\theta = 0.4$, with $\theta = 1$ being the total drying time. It can be seen that the average concentration increases in time as a consequence of droplet volume reduction, but also that the Péclet number has a significant effect on the concentration profile dynamics. The particle concentration is almost constantly homogeneous in the droplet for $Pe = 1$, because of the predominant effect of particle diffusivity over droplet shrinkage, whereas for larger Péclet, due to the lower diffusivity, the concentration rapidly increases at the

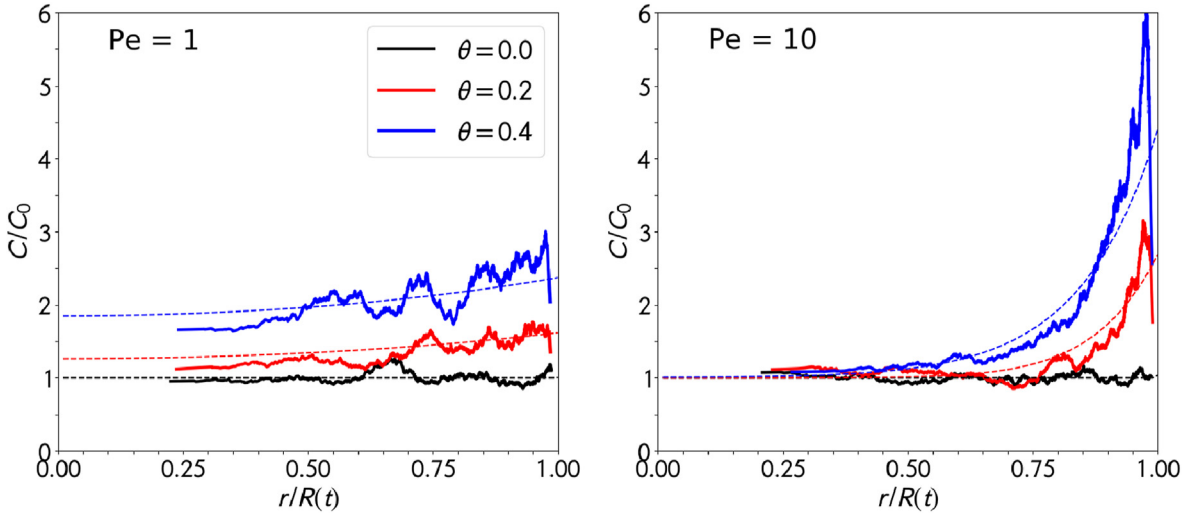

Fig. 5. Concentration profile in a shrinking droplet for different values of the dimensionless time obtained from DEM simulations (solid lines) and from the continuous model (dashed lines). Black, red and blue lines correspond to dimensionless times θ of 0.0, 0.2 and 0.4 respectively. Left: $Pe = 1$. Right: $Pe = 10$. (For interpretation of the references to color in this figure legend, the reader is referred to the Web version of this article.)

periphery of the droplet and a steep variation of the concentration profile can be observed along the radial coordinate r at any time θ.

The graphs also report the DEM predictions; here the concentration profiles were obtained by postprocessing data from 25 equivalent realizations of the process. The radius of the particles was 10 nm, the initial droplet radius was 0.215 μm and the volumic solid fraction was around 1%. Simulations at $Pe = 10$ and $Pe = 1$ were obtained by imposing a shrinkage time of 0.21 ms and 2.10 ms, respectively. The number concentration in the surrounding of each primary particle was calculated by considering the spherical shell that includes the 20 particles located immediately before and after the considered particle. The agreement between the continuous and discrete results is satisfactory, with the small discrepancies to be ascribed to the finite size of the particles in the DEM simulations compared to the droplet size, which necessarily induce some statistical noise in the data. Nevertheless, the agreement proves that our simulation strategy correctly predicted the particle collective behavior inside the droplets.

3.3. Breakup of agglomerates under elongational flow

We assessed the resistance of the agglomerates to fluid dynamic stresses by running Stokesian dynamics simulations. We placed two of the agglomerates produced by spray drying in an elongational flow of gradually increasing intensity. In this type of flow, the velocity gradient tensor at infinite distance from the agglomerate has only two non zero elements: $du_x/dx = -du_z/dz = \dot{\gamma}/2$. The equivalent shear rate $\dot{\gamma}$ is the square root of the second invariant of the velocity gradient tensor. The streamlines of the undisturbed flow are shown in the inset of Fig. 6. One of the clusters was taken from a population obtained at $Pe = 1$ (compact agglomerate), the other one from a population obtained at $Pe \to \infty$ (hollow agglomerate). The radius of the primary particles of both agglomerates was $a = 100$ nm. The structural properties of the agglomerates and contacts (ϱ_p, E, G, ν, γ_s) were the same as the ones used in the spray drying simulations and are reported in Table 1. The compact agglomerate was formed by 85 monomers and it initially had 177 interparticles contacts; the hollow cluster was made by 115 monomers with 185 initial interparticle contacts.

Contact forces are extremely sensitive to small changes in the relative position of the particles and even small departures from equilibrium give rise to extremely strong internal stresses. This is why, before studying the effect of the strength of the flow on the agglomerates, the two clusters were immersed in a stagnant field for 0.1 s and then in a low-strength elongational flow ($\mu\dot{\gamma} = 2$ Pa) for an additional time of 0.1 s. This procedure allowed the contacting particles to adjust their relative position by reaching their equilibrium separation, making the breakup simulations more stable. The effect of the strength of the flow on the clusters was investigated by prescribing an elongational field with strength $\mu\dot{\gamma}$ that was increased linearly at a constant rate of 5000 Pa/s from 0 Pa until breakup could be observed. A constant time step $\Delta t = 5 \cdot 10^{-8}$ s was adopted in the first-order explicit integration of the translational and rotational equations of motion of the primary particles.

The response to the fluid dynamic stress and the path to breakup were quite different for the two agglomerates considered, as made apparent in Fig. 6, where a series of snapshots of the clusters taken at subsequent times and increasing values of stress are given (the full video is available in the online Supplementary Material). The compact cluster (Fig. 6 top) remained almost completely undeformed until a few moments before rupture. In the very initial stage ($\mu\dot{\gamma} < 1000$ Pa) it rigidly rotated until aligned with the fluid velocity direction. Between 1000 and 4000 Pa there was no significant movement of the agglomerate neither deformation, except for the small sliding of few monomers on the surface of the cluster. At 4020 Pa the cluster began to deform significantly by stretching in the x-direction of the flow; rupture occurred immediately thereafter, at around 4040 Pa. As shown in Fig. 7 (left), the radius of gyration of the cluster did not change from the beginning of the application of the flow field until a few moments before rupture. In order to better characterize the geometry change, the cluster was also approximated by the triaxial ellipsoid with the same inertia tensor, and the shortest and longest semi-axes of this ellipsoid, which represent the characteristic sizes of the agglomerate [64,65] are plotted in Fig. 7 (left). These variables remained constant during the process, except for a small variation at 3000 Pa due to the partial sliding of single monomers. This behavior confirmed that the agglomerate was practically rigid until breakup, which therefore occurred in a brittle manner. The number of monomer-monomer contacts was 177 at the beginning of the simulation and remained constant at this value till 1500 Pa; after that, it increased slowly and steadily because of the compression in the z-direction until it reached 185 contacts shortly before breakup. The variation of the

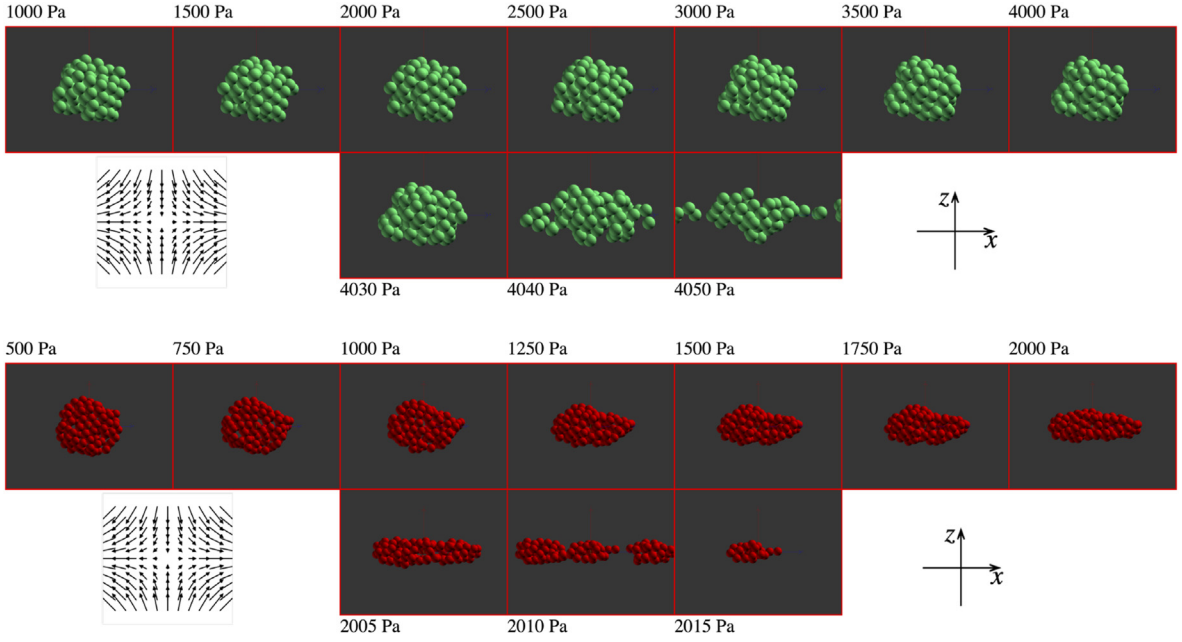

Fig. 6. Snapshot of the evolution up to breakup of a compact agglomerate (85 monomers) obtained by spray drying at $Pe = 1$ (above) and of a hollow agglomerate (115 monomers) obtained in the high Péclet limit (below) in an elongational flow of increasing strength $\mu\dot{\gamma}$. The undisturbed streamlines are shown in the inset.

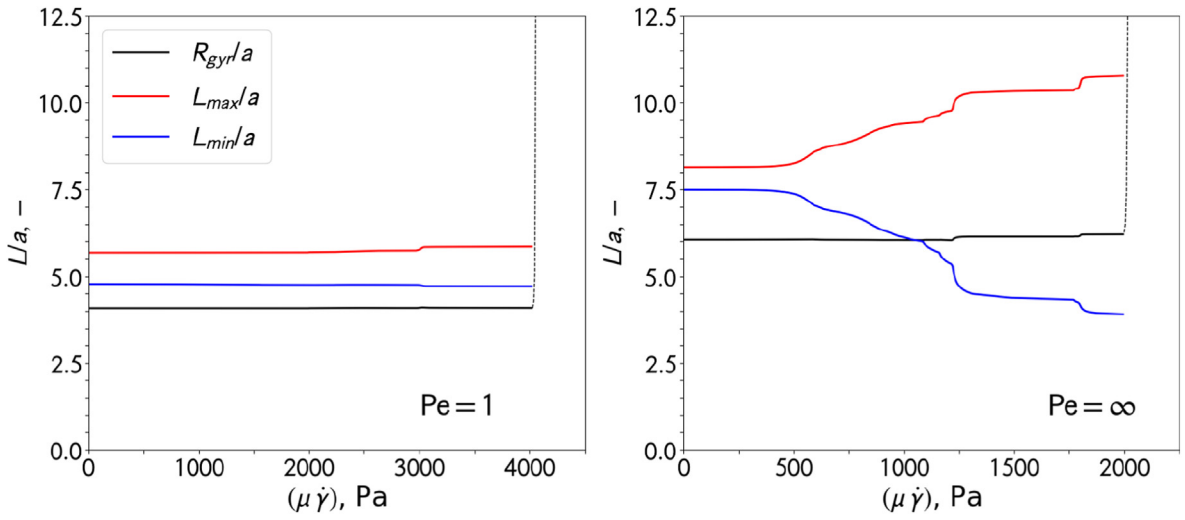

Fig. 7. Radius of gyration (black line); size of the largest (red) and smallest (blue) semiaxis of the equivalent ellipsoid for a compact cluster ($Pe = 1$, left), and for a hollow cluster ($Pe \to \infty$, right). The plot reports the temporal evolution of these quantities during the elongation process as a function of the applied fluid dynamic stress. The dashed line describes the sudden increase of the radius of gyration occurring after breakup. (For interpretation of the references to color in this figure legend, the reader is referred to the Web version of this article.)

average coordination number was extremely small, from 4.16 to 4.35, further showing that the structure of the agglomerate remained almost unchanged till breakup occurred.

In the hollow agglomerate the deformation of the structure before breakup was more significant (Fig. 6 bottom). Here too, there was an initial stage (up to 1000 Pa) of alignment with the flow field, but the structure remained rigid only up to about 600 Pa. At stresses larger than this, it began to flatten in the z-direction and to stretch in the x-direction. This effect is made quantitatively apparent by the change in the size of the semi-axes of the triaxial ellipsoid reported in Fig. 7 (right), where the largest semiaxis, aligned with x throughout the deformation process, increases, whereas the smallest one, aligned with z, decreases. It is worth to notice that the radius of gyration was unable to reflect this deformation phenomenon, because the simultaneous effect of compression along z and elongation along x balanced each other, such that the average distance of the primary particles from the center of mass of the cluster remained almost unchanged. Results also made apparent that the flattening effect made the structure more rigid and in fact between 1200 and 1800 Pa the cluster was not subject to further deformation. Around 1800 Pa restructuring started again further flattening the agglomerate; then the structure remained stable until rupture, which took place between 2005 and 2010 Pa. It must be noted that, during the entire process, the structure did not collapse on itself and the internal cavity was preserved. The variation in the number of inter-particle contacts was here significant. They remained constant at 183 up to 600 Pa, then increased steadily with the partial flattening of the structure up to 199 at 1400 Pa and finally remained again constant until rupture. The average coordination number is quite high, but smaller than the previous case, because of the presence of the cavity; it varied from 3.18 at the beginning of the process to 3.46 just before breakup.

In the used DEM approach, processes acting at very different scales had to be simulated simultaneously. Hydrodynamic interactions and the large scale motion of the agglomerate take place on lengths of the order of the size of the agglomerate, whereas contact forces and local deformations of the contact area act on distances that could be smaller than 1 nm. As a consequence, the time step had to be extremely small in comparison to the duration of the process and the simulations were very slow and required substantial computational resources. However, it was apparent that, because of the high coordination number and the strength of the internal bonds, the compact cluster behaved almost like a rigid body until rupture. This behavior suggested that the relevant information on the breakup of the agglomerate can be obtained by simpler and much less time-consuming simulations.

In the limit of small deformation and brittle fracture we can in fact apply the methods of the structural mechanics of rigid bodies to determine how the hydrodynamic forces are redistributed as contact stresses over the particle network. By comparing the internal force acting at each contact with the pull-off value required for severing the bond, one can then determine the hydrodynamic stress required for the occurrence of breakup. When the cluster is modeled as a rigid body, the dynamics of the system is determined only by the equations of motion of the whole agglomerate. The small scale motions at the intermolecular contacts, due to surface forces or local deformations, are not considered in the approach, making the problem much better conditioned. The approach was proposed originally for isostatic agglomerates [56] and then extended to hyperstatic agglomerates [57] and it has then applied to the dynamics of breakup in turbulent fluids [66] and in highly viscous systems [67,68].

In the rigid body assumption limit, we assumed that breakup occurs when the normal stress exceeds the pull-off force at any of the intermonomer bonds. The distribution of intermonomer stresses for the compact agglomerate is shown in Fig. 8 as a function of the radial distance from the center of mass. The highest tensile stress for the compact agglomerate was $N_{\max}/(6\pi\mu\dot{\gamma}a^2) = 2.89$, which was compared with the pull-off force given by Eq. (6). In this way, the critical shear stress for the breakup of the most stressed bond is $\mu\dot{\gamma}_{br} = 4120$ Pa, which compares considerably well with the value of 4040 Pa obtained by the complete DEM simulation. Most remarkably, and somehow unexpected, is what happened when the rigid DEM was applied to the hollow cluster (blue squares in Fig. 8). The largest value of dimensionless normal stress was $N_{\max}/(6\pi\mu\dot{\gamma}a^2) = 6.24$, which gives rise to a critical shear stress of 1930 Pa. Even in this case the prediction of the rigid DEM was more than satisfactory when contrasted with the value given by the rigorous DEM (2010 Pa), although the assumption of stiffness is not fully valid in this case and the agglomerate underwent some restructuring before breaking up. However, apparently, the restructuring was not strong enough to significantly change the structure of the agglomerate, which in fact preserved the central cavity and the cross-linked network of bonds until breakup. Therefore, the assumption of rigid body well predicted the different mechanical stability of the two classes of clusters, and it has been imposed for the subsequent simulations.

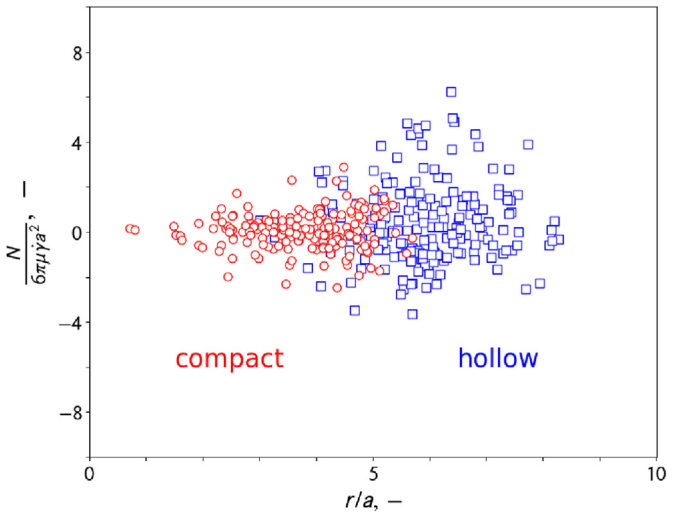

Fig. 8. Distribution of the normal stress at contact as a function of the distance r from the center of mass for the two agglomerates (compact and hollow) calculated from DEM under the rigid mody motion assumption. Compact agglomerate (red circles) and hollow agglomerate (blue squares). (For interpretation of the references to color in this figure legend, the reader is referred to the Web version of this article.)

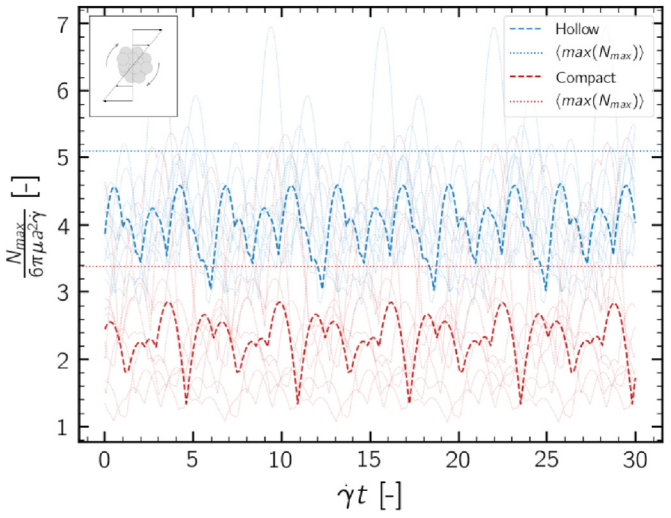

Fig. 9. Maximum tensile stress N_{max} acting inside a cluster in a planar shear flow. In the inset a qualitative representation of the simulation setup and of the shear flow is given. Blue curves: hollow clusters. Red curves: compact clusters. The horizontal dotted lines show the average value of the maximum tensile stress experienced by clusters of the two classes. (For interpretation of the references to color in this figure legend, the reader is referred to the Web version of this article.)

3.4. Compact and hollow agglomerates under shear flow

Rigid DEM simulations in shear flow were conducted for a population of 10 compact agglomerates produced at $Pe = 1$ and 10 hollow agglomerates produced at $Pe \to \infty$ with size of primary particles $a = 100$ nm. In shear flow, the only non-zero component of the velocity gradient was $\dot{\gamma} = du_x/dy$ (with $\dot{\gamma}$ being the shear rate for this case). In shear, both rotational and elongational components of the flow are present, such that the aggregate, as it rotates, undergoes periodically traction along the $+45°$ axis (w.r.t. the flow direction) and compression along the $-45°$ direction. As already commented, the physical deformation process leading to breakup through restructuring and detachment of fragments is not simulated under the condition of rigid body motion; however, valuable insights about the distribution of the contact forces inside the clusters can be obtained and the mechanical stability of the two classes can be compared.

Fig. 9 shows the instantaneous value of the maximum tensile force N_{max} acting inside clusters suspended in a shear flow with constant shear rate $\dot{\gamma}$. Both time and maximum tensile stress are made dimensionless, exploiting the linearity between internal contact forces and applied hydrodynamic stress valid in the elastic regime. Each line refers to a single simulation and one arbitrary line for each class is highlighted to show the typical trend followed by N_{max} in a shear flow. The oscillation of N_{max} is due to the rigid rotation of the cluster, which exposes periodically different bonds to the orientation of maximum traction. The two horizontal lines represent the maximum tensile stress experienced by a cluster along its whole path, averaged over the entire simulation set. The dimensionless value for hollow clusters and compact clusters was around 5.1 and 3.3, respectively. Such values correspond to a critical fluid dynamic shear stress $\mu\dot{\gamma}$ of 2360 Pa and 3650 Pa, respectively. Therefore, as observed in elongational flow, hollow clusters experienced higher internal tensile forces, meaning that they are easier to break. Compact clusters instead are stronger. This latter class of agglomerate has in fact a more over-constrained structure, in which every particle is bonded to a higher number of other particles; therefore, mechanical stresses are uniformly discharged over the neighboring particles and do not accumulate in few critical locations. This makes compact clusters to better resist hydrodynamic stresses.

3.5. Computational effort

All the simulations were run on a workstation equipped with a Intel(R) Xeon(R) CPU E5-2630 v4 @ 2.20 GHz. A single drop drying simulation required approximately 30 h in the high Péclet regime and approximately 10 days in the low Péclet regime. The simulations of agglomerate dispersion of Section 3.3 were run using 8 OpenMP threads and each of them required approximately 7 days. The rigid body approximation was highly beneficial for the computational cost of the simulations of internal stresses: the computational time per simulation dropped to few minutes.

4. Conclusions

This work investigated the formation of agglomerates in a spray drying process and their mechanical response in terms of restructuring and breakup when subject to an externally imposed flow field. Results provided several significant insights about the experimental conditions required to design clusters able to resist or to undergo breakup.

In the DEM simulation of a single-droplet spray drying process, we observed different possible outcomes of the process in terms of generated morphology. The main governing factor emerged to be the Péclet number, i.e., the ratio between the shrinkage time and the diffusion time; spray drying simulations conducted in condition of low Péclet number led to the formation of compact spherical agglomerates with a uniform density, whereas, in condition of high Péclet number, hollow agglomerates were obtained. We also observed that in the high Péclet limit no significant morphology changes were induced by variation of the evaporation time. The role of other investigated factors, such as monomer size and initial solid fraction, was minor in comparison to Pe in determining the structural features of the agglomerates.

The mechanical response of the agglomerates generated by the drying process were analyzed in terms of restructuring and fragmentation behaviour by a DEM code based on Stokesian dynamics and incorporating a model for properly counting for both van der Waals and contact forces. This part of the study was performed to study the response of different types of agglomerates to an elongational and a shear flow field.

Two representative morphologies (a compact agglomerate obtained for $Pe = 1$ and a hollow agglomerate obtained for $Pe \to \infty$) were placed in an elongational flow field of linearly increasing intensity. Compact and hollow agglomerates emerged to undergo a different path to breakup and furthermore it has been observed that the compact agglomerate has a hydrodynamic breakup stress $\mu\dot{\gamma}$ that was twice as high as that of the hollow one. Analogous results were obtained by investigating the maximum tensile stresses acting inside a population of rigid hollow agglomerates and rigid compact agglomerates suspended in a shear flow. Furthermore, we observed that compact clusters are subject to brittle rupture. They remained rigid without noticeable deformation until a few moments before breakup; in hollow agglomerates, on the other hand, there was a certain level of deformation before breakup occurred which, however, did not alter the structural characteristics of the cluster: the cavity was in fact preserved and the coordination number of the monomers did not vary excessively up to the occurrence of breakup. The consequence is that, in both cases, a simple analysis of the stresses acting on the agglomerates, neglecting the deformations (i.e. considering the agglomerate as rigid), is sufficient to provide useful information about the breakup occurrence.

Finally, it is worth to mention that the DEM predictions for the spray drying process were obtained under a few working hypotheses. We assumed in fact that the evaporation occurred at constant and uniform temperature, and we did not address the effect of the forming surface crust, which can possibly change the rate of heat and mass transfer, thus modifying the shrinking rate and the temperature dynamics. Furthermore, we did not include in our model the full DLVO theory nor the lubrication interaction between the particles, under the assumption that capillary forces are strong enough to overcome any resistance to aggregation. Future work should however aim at overcoming these limitations and embed such features in DEM simulations. The detailed modeling of heat and mass transfer and of the colloidal interactions between particles can in fact possibly contribute to explain some of the experimentally observed behavior (such as the crust instability and possible fragmentation) and provide one with the information needed to select the particle physico-chemical properties for obtaining agglomerate with predictable morphologies. Further insights into the process can also be obtained by a characterization of the equipment flow field and droplet interaction, possibly achievable by computational fluid dynamics and population balance models describing the disperse phase population dynamics.

Fundings

This research did not receive any specific grant from funding agencies in the public, commercial, or not-for-profit sectors.

Authors' contributions

Lorenzo Vasquez Giuliano: Methodology, Software, Investigation, Formal analysis, Writing-Original Draft. Antonio Buffo: Supervision, Resources. Marco Vanni: Supervision, Project administration. Graziano Frungieri: Conceptualization, Methodology, Supervision, Writing - Review & Editing.

Declaration of competing interest

The authors declare that they have no known competing financial interests or personal relationships that could have appeared to influence the work reported in this paper.

Data availability

Data will be made available on request.

Acknowledgements

G. F. gratefully acknowledges support from the "TUM Global Postdoc Fellowship" program.

Appendix A. Supplementary data

Supplementary data to this article can be found online at https://doi.org/10.1016/j.jciso.2022.100068.

References

[1] D.-L. Yang, Q. Sun, Y.-H. Duan, H. Niu, R.-L. Wang, D. Wang, M.-F. Zhu, J.-X. Wang, Efficient construction of SiO_2 colloidal nanoparticle clusters as novel fillers by a spray-drying process for dental composites, Ind. Eng. Chem. Res. 58 (2019) 18178–18186, https://doi.org/10.1021/acs.iecr.9b02720.

[2] A. Mishra, V.K. Pandey, B.S. Shankar, J.S. Melo, Spray drying as an efficient route for synthesis of silica nanoparticles-sodium alginate biohybrid drug carrier of doxorubicin, Colloids Surf. B Biointerfaces 197 (2021), 111445, https://doi.org/10.1016/j.colsurfb.2020.111445.

[3] L. Ruffel, J. Soulié, Y. Coppel, P. Roblin, F. Brouillet, C. Frances, M. Tourbin, Ibuprofen loading into mesoporous silica nanoparticles using co-spray drying: a multi-scale study, Microporous Mesoporous Mater. 291 (2020), 109689, https://doi.org/10.1016/j.micromeso.2019.109689.

[4] N. Tsapis, D. Bennett, B. Jackson, D.A. Weitz, D.A. Edwards, Trojan particles: large porous carriers of nanoparticles for drug delivery, Proc. Natl. Acad. Sci. USA 99 (2002) 12001–12005, https://doi.org/10.1073/pnas.18223399.

[5] M. Barasinski, C. Schilde, S. Melzig, M. Hübner, G. Garnweitner, S. Zellmer, Micromechanical properties of spray-dried core-shell silica aggregates along with drug release tests, JCIS Open 6 (2022), 100052, https://doi.org/10.1016/j.jciso.2022.100052.

[6] P. Roy, G. Bertrand, C. Coddet, Spray drying and sintering of zirconia based hollow powders, Powder Technol. 157 (2005) 20–26, https://doi.org/10.1016/j.powtec.2005.05.031.

[7] G. Bertrand, P. Roy, C. Filiatre, C. Coddet, Spray-dried ceramic powders: a quantitative correlation between slurry characteristics and shapes of the granules, Chem. Eng. Sci. 60 (2005) 95–102, https://doi.org/10.1016/j.ces.2004.04.042.

[8] R. Zhang, Q. Tan, S. Bao, J. Deng, Y. Xie, F. Zheng, G. Wu, B. Xu, Spray drying induced engineering a hierarchical reduced graphene oxide supported heterogeneous tin dioxide and zinc oxide for lithium-ion storage, J. Colloid Interface Sci. 608 (2022) 1758–1768, https://doi.org/10.1016/j.jcis.2021.10.026.

[9] G. Liu, Z. Wang, B. Bao, Z. Ouyang, C. Du, F. Liu, W. Wang, D. Yu, Construction of sustainable and multifunctional polyester fabrics via an efficiently and eco-friendly spray-drying layer-by-layer strategy, J. Colloid Interface Sci. 588 (2021) 50–61, https://doi.org/10.1016/j.jcis.2020.12.049.

[10] I. Schmitz-Schug, U. Kulozik, P. Foerst, Modeling spray drying of dairy products–impact of drying kinetics, reaction kinetics and spray drying conditions on lysine loss, Chem. Eng. Sci. 141 (2016) 315–329, https://doi.org/10.1016/j.ces.2015.11.008.

[11] A.B.D. Nandiyanto, K. Okuyama, Progress in developing spray-drying methods for the production of controlled morphology particles: from the nanometer to submicrometer size ranges, Adv. Powder Technol. 22 (2011) 1–19, https://doi.org/10.1016/j.apt.2010.09.011.

[12] A. Stunda-Zujeva, Z. Irbe, L. Berzina-Cimdina, Controlling the morphology of ceramic and composite powders obtained via spray drying – a review, Ceram. Int. 43 (2017) 11543–11551, https://doi.org/10.1016/j.ceramint.2017.05.023.

[13] R. Mondal, A. Das, D. Sen, D.K. Satapathy, M.G. Basavaraj, Spray drying of colloidal dispersions containing ellipsoids, J. Colloid Interface Sci. 551 (2019) 242–250, j.jcis.2019.05.012.

[14] S. Schyck, J.-M. Meijer, L. Baldauf, P. Schall, A.V. Petukhov, L. Rossi, Self-assembly of colloidal superballs under spherical confinement of a drying droplet, JCIS Open 5 (2022), 100037, https://doi.org/10.1016/j.jciso.2021.100037.

[15] R. Mondragon, L. Hernandez, J.E. Julia, J.C. Jarque, S. Chiva, B. Zaitone, C. Tropea, Study of the drying behavior of high load multiphase droplets in an acoustic levitator at high temperature conditions, Chem. Eng. Sci. 66 (2011) 2734–2744, https://doi.org/10.1016/j.ces.2011.03.033.

[16] A. Osman, L. Goehring, A. Patti, H. Stitt, N. Shokri, Fundamental investigation of the drying of solid suspensions, Ind. Eng. Chem. Res. 56 (2017) 10506–10513, https://doi.org/10.1021/acs.iecr.7b02334.

[17] J.C. Lin, J.W. Gentry, Spray drying drop morphology: experimental study, Aerosol Sci. Technol. 37 (2003) 15–32, https://doi.org/10.1080/02786820300888.

[18] E. Boel, R. Koekoekx, S. Dedroog, I. Babkin, M.R. Vetrano, C. Clasen, G. Van den Mooter, Unraveling particle formation: from single droplet drying to spray drying and electrospraying, Pharmaceutics 12 (2020) 625, https://doi.org/10.3390/pharmaceutics12070625.

[19] E. Lintingre, F. Lequeux, L. Talini, N. Tsapis, Control of particle morphology in the spray drying of colloidal suspensions, Soft Matter 12 (2016) 7435–7444, https://doi.org/10.1039/C6SM01314G.

[20] N. Tsapis, E.R. Dufresne, S.S. Sinha, C.S. Riera, J.W. Hutchinson, L. Mahadevan, D.A. Weitz, Onset of buckling in drying droplets of colloidal suspensions, Phys. Rev. Lett. 94 (1) (2005), 018302, https://doi.org/10.1103/PhysRevLett.94.018302.

[21] D. Pramudita, E. Tsotsas, A model of pulse combustion drying and breakup of colloidal suspension droplets, Powder Technol. 355 (2019) 755–769, https://doi.org/10.1016/j.powtec.2019.07.096.

[22] D. Pramudita, A. Teiwes, M. Jacob, E. Tsotsas, Crust breakage in production of fine particles using pulse combustion drying: experimental and numerical investigations, Powder Technol. 393 (2021) 77–98, https://doi.org/10.1016/j.powtec.2021.07.060.

[23] D. Pramudita, S. Humjaa, E. Tsotsas, Droplet drying and whey protein denaturation in pulsed gas flow-a modeling study, J. Food Eng. 321 (2022), 110959, https://doi.org/10.1016/j.jfoodeng.2022.110959.

[24] S. Zellmer, G. Garnweitner, T. Breinlinger, T. Kraft, C. Schilde, Hierarchical structure formation of nanoparticulate spray-dried composite aggregates, ACS Nano 9 (2015) 10749–10757, https://doi.org/10.1021/acsnano.5b05220.

[25] K. Jabłczyńska, J.M. Gac, T.R. Sosnowski, Self-organization of colloidal particles during drying of a droplet: modeling and experimental study, Adv. Powder Technol. 29 (2018) 3542–3551, https://doi.org/10.1016/j.apt.2018.09.036.

[26] C.S. Handscomb, M. Kraft, A.E. Bayly, A new model for the drying of droplets containing suspended solids after shell formation, Chem. Eng. Sci. 64 (2009) 228–246, https://doi.org/10.1016/j.ces.2008.10.019.

[27] C.S. Handscomb, M. Kraft, Simulating the structural evolution of droplets following shell formation, Chem. Eng. Sci. 65 (2010) 713–725, https://doi.org/10.1016/j.ces.2008.10.019.

[28] H. Abdullahi, C.L. Burcham, T. Vetter, A mechanistic model to predict droplet drying history and particle shell formation in multicomponent systems, Chem. Eng. Sci. 224 (2020), 115713, https://doi.org/10.1016/j.ces.2020.115713.

[29] T. Breinlinger, A. Hashibon, T. Kraft, Simulation of the influence of surface tension on granule morphology during spray drying using a simple capillary force model, Powder Technol. 283 (2015) 1–8, https://doi.org/10.1016/j.powtec.2015.05.009.

[30] G. Frungieri, M. Vanni, Shear-induced aggregation of colloidal particles: a comparison between two different approaches to the modelling of colloidal interactions, Can. J. Chem. Eng. 95 (2017) 1768–1780, https://doi.org/10.1002/cjce.22843.

[31] B. Faure, B. Jesper Sæderup Lindeløv, M. Wahlberg, N. Adkins, P. Jackson, L. Bergström, Spray drying of TiO_2 nanoparticles into redispersible granules, Powder Technol. 203 (2010) 384–388, https://doi.org/10.1016/j.powtec.2010.05.033.

[32] T. Lebhardt, S. Roesler, H.P. Uusitalo, T. Kissel, Surfactant-free redispersible nanoparticles in fast-dissolving composite microcarriers for dry-powder inhalation, Eur. J. Pharm. Biopharm. 78 (2011) 90–96, https://doi.org/10.1016/j.ejpb.2010.12.002.

[33] K. Kho, K. Hadinoto, Aqueous re-dispersibility characterization of spray-dried hollow spherical silica nano-aggregates, Powder Technol. 198 (2010) 354–363, https://doi.org/10.1016/j.powtec.2009.11.031.

[34] A. Marie, M. Tourbin, A.-C. Robisson, C. Ablitzer, C. Frances, Wet size measurements for the evaluation of the deagglomeration behaviour of spray-dried alumina powders in suspension, Ceram. Int. 48 (6) (2022) 7926–7936, https://doi.org/10.1016/j.ceramint.2021.11.340.

[35] K. Kho, K. Hadinoto, Effects of excipient formulation on the morphology and aqueous re-dispersibility of dry-powder silica nano-aggregates, Colloids Surf. A Physicochem. Eng. Asp. 359 (2010) 71–81, https://doi.org/10.1016/j.colsurfa.2010.01.066.

[36] G. Frungieri, M. Vanni, Aggregation and breakup of colloidal particle aggregates in shear flow: a combined Monte Carlo - Stokesian dynamics approach, Powder Technol. 388 (2021) 357–370, https://doi.org/10.1016/j.powtec.2021.04.076.

[37] L. Guérin, C. Coufort-Saudejaud, A. Liné, C. Frances, Dynamics of aggregate size and shape properties under sequenced flocculation in a turbulent taylor-Couette reactor, J. Colloid Interface Sci. 491 (2017) 167–178, https://doi.org/10.1016/j.jcis.2016.12.042.

[38] N. Korin, M. Kanapathipillai, B.D. Matthews, M. Crescente, A. Brill, T. Mammoto, K. Ghosh, S. Jurek, S.A. Bencherif, D. Bhatta, et al., Shear-activated nanotherapeutics for drug targeting to obstructed blood vessels, Science 337 (2012) 738–742, https://doi.org/10.1126/science.1217815.

[39] L. Vasquez Giuliano, A. Buffo, M. Vanni, A.S. Lanotte, V. Arima, M. Bianco, F. Baldassarre, G. Frungieri, Response of shear-activated nanotherapeutic particles in a clot-obstructed blood vessel by CFD-DEM simulations, Can. J. Chem. Eng. 100 (2022) 3562–3574, https://doi.org/10.1002/cjce.24502.

[40] M.L. Eggersdorfer, D. Kadau, H.J. Herrmann, S.E. Pratsinis, Fragmentation and restructuring of soft agglomerates under shear, J. Colloid Interface Sci. 342 (2010) 261–268, https://doi.org/10.1016/j.jcis.2009.10.062.

[41] Y.M. Harshe, M. Lattuada, Universal breakup of colloidal clusters in simple shear flow, J. Phys. Chem. B 120 (2016) 7244–7252, https://doi.org/10.1021/acs.jpcb.6b03220.

[42] V. Šmilauer, E. Catalano, B. Chareyre, S. Dorofeenko, J. Duriez, A. Gladky, J. Kozicki, C. Modenese, L. Scholtès, L. Sibille, et al., Yade Documentation, third ed., The Yade Project, 2015.

[43] L. Turetta, M. Lattuada, Brownian dynamics simulations of shear-induced aggregation of charged colloidal particles in the presence of hydrodynamic interactions, J. Colloid Interface Sci. 624 (2022) 637–649, https://doi.org/10.1016/j.jcis.2022.05.047.

[44] L. Turetta, M. Lattuada, The role of hydrodynamic interactions on the aggregation kinetics of sedimenting colloidal particles, Soft Matter 18 (8) (2022) 1715–1730, https://doi.org/10.1039/D1SM01637G.

[45] V. Becker, E. Schlauch, M. Behr, H. Briesen, Restructuring of colloidal aggregates in shear flows and limitations of the free-draining approximation, J. Colloid Interface Sci. 339 (2) (2009) 362–372, https://doi.org/10.1016/j.jcis.2009.07.022.

[46] M. Kroupa, M. Vonka, J. Kosek, Modeling the mechanism of coagulum formation in dispersions, Langmuir 30 (2014) 2693–2702, https://doi.org/10.1021/la500101x.

[47] J.F. Wilson, M. Kroupa, J. Kosek, M. Soos, Numerical study of soft colloidal nanoparticles interaction in shear flow, Langmuir 34 (2018) 15600–15611, https://doi.org/10.1021/acs.langmuir.8b03350.

[48] X. Ruan, S. Chen, S. Li, Structural evolution and breakage of dense agglomerates in shear flow and Taylor-Green vortex, Chem. Eng. Sci. 211 (2020), 115261, https://doi.org/10.1016/j.ces.2019.115261.

[49] P.S. Grassia, E.J. Hinch, L.C. Nitsdche, Computer simulations of Brownian motion of complex systems, J. Fluid Mech. 282 (1995) 373–403, https://doi.org/10.1017/S0022112095000176.

[50] P.A. Cundall, O.D.L. Strack, A discrete numerical model for granular assemblies, Geotechnique 29 (1979) 47–65, https://doi.org/10.1680/geot.1979.29.1.47.

[51] K.L. Johnson, K. Kendall, A.D. Roberts, Surface energy and the contact of elastic solids, Proc. Roy. Soc. Lond.. Math. Phys. Sci. 324 (1971) 301–313, https://doi.org/10.1098/rspa.1971.0141.

[52] B. Harthong, J.-F. Jerier, V. Richefeu, B. Chareyre, P. Dorémus, D. Imbault, F.-V. Donzé, Contact impingement in packings of elastic–plastic spheres, application to powder compaction, Int. J. Mech. Sci. 61 (2012) 32–43, https://doi.org/10.1016/j.ijmecsci.2012.04.013.

[53] R.A. Hosn, L. Sibille, N. Benahmed, B. Chareyre, Discrete numerical modeling of loose soil with spherical particles and interparticle rolling friction, Granul. Matter 19 (2017) 1–12, https://doi.org/10.1007/s10035-016-0687-0.

[54] A.L. Yarin, G. Brenn, O. Kastner, C. Tropea, Drying of acoustically levitated droplets of liquid–solid suspensions: evaporation and crust formation, Phys. Fluids 14 (2002) 2289–2298, https://doi.org/10.1063/1.1483308.

[55] G. Frungieri, M.U. Bäbler, M. Vanni, Shear-induced heteroaggregation of oppositely charged colloidal particles, Langmuir 36 (2020) 10739–10749, https://doi.org/10.1021/acs.langmuir.0c01536.

[56] M. Vanni, A. Gastaldi, Hydrodynamic forces and critical stresses in low-density aggregates under shear flow, Langmuir 27 (2011) 12822–12833, https://doi.org/10.1017/S002211208700171X.

[57] M. Vanni, Accurate modelling of flow induced stresses in rigid colloidal aggregates, Comput. Phys. Commun. 192 (2015) 70–90, https://doi.org/10.1016/j.cpc.2015.02.022.

[58] Z. Ren, Y.M. Harshe, M. Lattuada, Influence of the potential well on the breakage rate of colloidal aggregates in simple shear and uniaxial extensional flows, Langmuir 31 (2015) 5712–5721, https://doi.org/10.1021/la504966y.

[59] L. Durlofsky, J.F. Brady, G. Bossis, Dynamic simulation of hydrodynamically interacting particles, J. Fluid Mech. 180 (1987) 21–49, https://doi.org/10.1017/S002211208700171X.

[60] J.S. Marshall, Discrete-element modeling of particulate aerosol flows, J. Comput. Phys. 228 (2009) 1541–1561, https://doi.org/10.1016/j.jcp.2008.10.035.

[61] C. Dominik, A.G.G.M. Tielens, The physics of dust coagulation and the structure of dust aggregates in space, Astrophys. J. 480 (1997) 647–673, https://doi.org/10.1086/303996.

[62] K. Bagi, M.R. Kuhn, A definition of particle rolling in a granular assembly in terms of particle translations and rotations, J. Appl. Mech. 71 (2004) 493–501, https://doi.org/10.1115/1.1755693.

[63] J. Cranck, The Mathematics of Diffusion, Clarendon Press, 1979.

[64] Y.M. Harshe, L. Ehrl, M. Lattuada, Hydrodynamic properties of rigid fractal aggregates of arbitrary morphology, J. Colloid Interface Sci. 352 (2010) 87–98, https://doi.org/10.1016/j.jcis.2010.08.040.

[65] L. Sanchez Fellay, C. Twist, M. Vanni, Motion of rigid aggregates under different flow conditions, Acta Mech. 224 (2013) 2225–2248, https://doi.org/10.1007/s00707-013-0928-9.

[66] J. De Bona, A.S. Lanotte, M. Vanni, Internal stresses and breakup of rigid isostatic aggregates in homogeneous and isotropic turbulence, J. Fluid Mech. 755 (2014) 365–396, https://doi.org/10.1017/jfm.2014.421.

[67] G. Frungieri, G. Boccardo, A. Buffo, D. Marchisio, H.A. Karimi-Varzaneh, M. Vanni, A CFD-DEM approach to study the breakup of fractal agglomerates in an internal mixer, Can. J. Chem. Eng. 98 (2020) 1880–1892, https://doi.org/10.1002/cjce.23773.

[68] G. Frungieri, G. Boccardo, A. Buffo, H.A. Karimi-Varzaneh, M. Vanni, CFD-DEM characterization and population balance modelling of a dispersive mixing process, Chem. Eng. Sci. 260 (2022), 117859, https://doi.org/10.1016/j.ces.2022.117859.